

Superconducting qubit-oscillator circuit beyond the ultrastrong-coupling regime

Fumiki Yoshihara,^{*} Tomoko Fuse,[†] and Kouichi Semba[‡]

*National Institute of Information and Communications Technology,
4-2-1, Nukuikitamachi, Koganei, Tokyo 184-8795, Japan*

Sahel Ashhab[§]

*Qatar Environment and Energy Research Institute,
Hamad Bin Khalifa University, Qatar Foundation, Doha, Qatar*

Kosuke Kakuyanagi and Shiro Saito

*NTT Basic Research Laboratories, NTT Corporation,
3-1 Morinosato-Wakamiya, Atsugi, Kanagawa 243-0198, Japan*

Abstract

The interaction between an atom and the electromagnetic field inside a cavity¹⁻⁶ has played a crucial role in the historical development of our understanding of light-matter interaction and is a central part of various quantum technologies, such as lasers and many quantum computing architectures. The emergence of superconducting qubits^{7,8} has allowed the realization of strong^{9,10} and ultrastrong¹¹⁻¹³ coupling between artificial atoms and cavities. If the coupling strength g becomes as large as the atomic and cavity frequencies (Δ and ω_o respectively), the energy eigenstates including the ground state are predicted to be highly entangled¹⁴. This qualitatively new regime can be called the deep strong-coupling regime¹⁵, and there has been an ongoing debate¹⁶⁻¹⁸ over whether it is fundamentally possible to realize this regime in realistic physical systems. By inductively coupling a flux qubit and an LC oscillator via Josephson junctions, we have realized circuits with g/ω_o ranging from 0.72 to 1.34 and $g/\Delta \gg 1$. Using spectroscopy measurements, we have observed unconventional transition spectra, with patterns resembling masquerade masks, that are characteristic of this new regime. Our results provide a basis for ground-state-based entangled-pair generation and open a new direction of research on strongly correlated light-matter states in circuit-quantum electrodynamics.

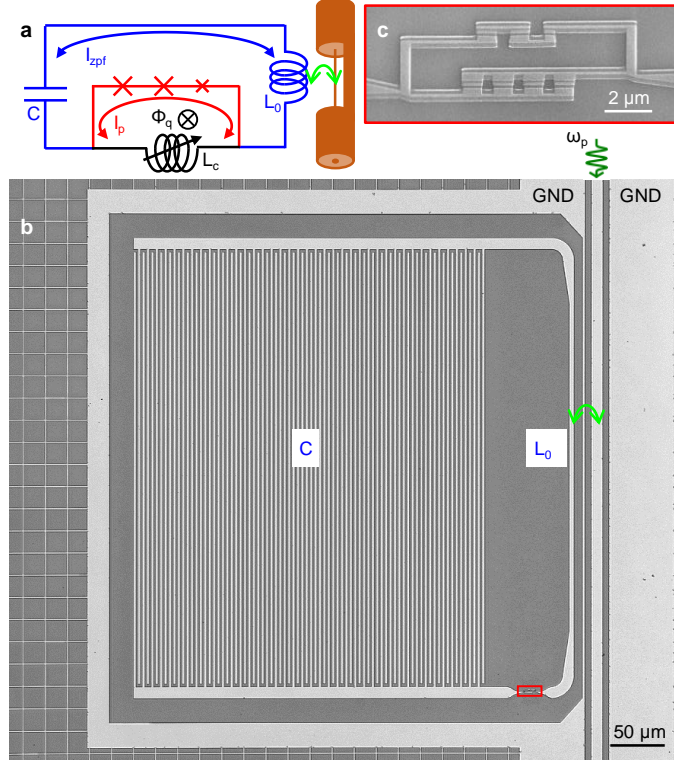


FIG. 1. **Superconducting qubit-oscillator circuit.** **a**, Circuit diagram. A superconducting flux qubit (red and black) and a superconducting LC oscillator (blue and black) are inductively coupled to each other by sharing a tunable inductance (black). **b**, Laser microscope image of the lumped-element LC oscillator inductively coupled to a coplanar transmission line. **c**, Scanning electron microscope image of the qubit and the coupler junctions located at the red rectangle in image **b**. The coupler, consisting of four parallel Josephson junctions, is tunable via the magnetic flux bias through its loops (see Supplementary Information, sections S1 and S2, and Fig. S1).

We begin by describing the Hamiltonian of each component in the qubit-oscillator circuit, which comprises a superconducting flux qubit and an LC oscillator inductively coupled to each other by sharing a tunable inductance L_c , as shown in the circuit diagram in Fig. 1a.

The Hamiltonian of the flux qubit can be written in the basis of two states with persistent currents flowing in opposite directions around the qubit loop¹⁹, $|L\rangle_q$ and $|R\rangle_q$, as $\mathcal{H}_q = -\hbar(\Delta\sigma_x + \varepsilon\sigma_z)/2$, where $\hbar\Delta$ and $\hbar\varepsilon = 2I_p\Phi_0(n_{\phi q} - n_{\phi q0})$ are the tunnel splitting and the energy bias between $|L\rangle_q$ and $|R\rangle_q$, I_p is the maximum persistent current, and $\sigma_{x,z}$ are Pauli matrices. Here, $n_{\phi q}$ is the normalized flux bias through the qubit loop in units of the superconducting flux quantum, $\Phi_0 = h/2e$, and $n_{\phi q0} = 0.5 + k_q$, where k_q is the integer

that minimizes $|n_{\phi q} - n_{\phi q 0}|$. The macroscopic nature of the persistent-current states enables strong coupling to other circuit elements. Another important feature of the flux qubit is its strong anharmonicity: the two lowest energy levels are well isolated from the higher levels.

The Hamiltonian of the LC oscillator can be written as $\mathcal{H}_o = \hbar\omega_o(\hat{a}^\dagger\hat{a} + 1/2)$, where $\omega_o = 1/\sqrt{(L_0 + L_{qc})C}$ is the resonance frequency, L_0 is the inductance of the superconducting lead, $L_{qc}(\simeq L_c)$ is the inductance across the qubit and coupler (see Supplementary Information, section S2), C is the capacitance, and \hat{a} (\hat{a}^\dagger) is the oscillator's annihilation (creation) operator. Figure 1b shows a laser microscope image of the lumped-element LC oscillator, where L_0 is designed to be as small as possible to maximize the zero-point fluctuations in the current $I_{zpf} = \sqrt{\hbar\omega_o/2(L_0 + L_{qc})}$ and hence achieve strong coupling to the flux qubit, while C is adjusted so as to achieve a desired value of ω_o . The freedom of choosing L_0 for large I_{zpf} is one of the advantages of lumped-element LC oscillators over coplanar-waveguide resonators for our experiment. Another advantage is that a lumped-element LC oscillator has only one resonant mode. Together with the strong anharmonicity of the flux qubit, we can expect that our circuit will realize the Rabi model^{20–23}, which is one of the simplest possible quantum models of qubit-oscillator systems, with no additional energy levels in the range of interest.

The coupling Hamiltonian can be written as⁹ $\mathcal{H}_c = \hbar g\sigma_z(\hat{a} + \hat{a}^\dagger)$, where $\hbar g = MI_p I_{zpf}$ is the coupling energy and $M(\simeq L_c)$ is the mutual inductance between the qubit and the LC oscillator. Importantly, a Josephson-junction circuit is used as a large inductive coupler²⁴ (Fig. 1c), which together with the large I_p and I_{zpf} allows us to achieve deep strong coupling.

The total Hamiltonian of the circuit is then given by

$$\mathcal{H}_{\text{total}} = -\frac{\hbar}{2}(\Delta\sigma_x + \varepsilon\sigma_z) + \hbar\omega_o(\hat{a}^\dagger\hat{a} + \frac{1}{2}) + \hbar g\sigma_z(\hat{a} + \hat{a}^\dagger). \quad (1)$$

Nonlinearities in the coupler circuit lead to higher-order terms in $(\hat{a} + \hat{a}^\dagger)$. The leading-order term can be written as $C_{A2}\hbar g(\hat{a} + \hat{a}^\dagger)^2$ and is known as the A^2 term¹⁶ in atomic physics. Since this A^2 term can be eliminated from $\mathcal{H}_{\text{total}}$ by a variable transformation (see Methods), we do not explicitly keep it and instead use Eq. (1) for our data analysis.

Spectroscopy was performed by measuring the transmission spectrum through a coplanar transmission line that is inductively coupled to the LC oscillator (see Supplementary Information, section S3). For a systematic study of the g dependence, five flux bias points in three circuits were used. Circuit II is designed to have larger values of g than the other two, and

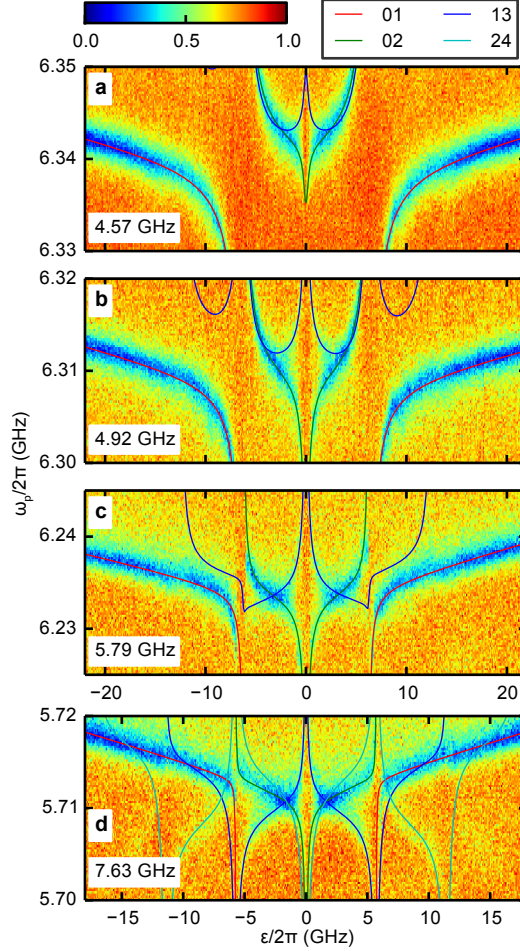


FIG. 2. **Transmission spectra for circuits I and II.** Calculated transition frequencies ω_{ij}^{cal} are superimposed on the experimental results. As summarized in Table I, panel **a** shows data from circuit I at $n_{\phi_q} = -0.5$, panel **b** shows data from circuit I at $n_{\phi_q} = -1.5$, panel **c** shows data from circuit I at $n_{\phi_q} = 2.5$, and panel **d** shows data from circuit II at $n_{\phi_q} = -0.5$. The values of $g/2\pi$ are written in the panels. The red, green, blue, and cyan lines indicate the transitions $|0\rangle \rightarrow |1\rangle$, $|0\rangle \rightarrow |2\rangle$, $|1\rangle \rightarrow |3\rangle$, and $|2\rangle \rightarrow |4\rangle$, respectively.

circuits I and II are designed to have smaller values of Δ than circuit III. Figures 2**a-d** show normalized amplitudes of the transmission spectra $|S_{21}(\omega_p)|/|S_{21}(\omega_p)|_{\text{max}}$ from circuits I and II as functions of the flux bias ε and probe frequency ω_p (see also Supplementary Information, Figs. S5**a-d**). Characteristic patterns resembling masquerade masks can be seen around $\varepsilon = 0$. At each value of ε , the spectroscopy data was fitted with Lorentzians to obtain the frequencies ω_{ij} of the transitions $|i\rangle \rightarrow |j\rangle$, where the indices i and j label the energy eigenstates according to their order in the energy-level ladder, with the index 0 denoting the

TABLE I. **Set of parameters obtained from fitting spectroscopy measurements.**

circuit	n_{ϕ_q}	Figure	$\Delta/2\pi$ (GHz)	$\omega_o/2\pi$ (GHz)	$g/2\pi$ (GHz)	$\alpha = g/\omega_o$	$2g/\sqrt{\omega_o\Delta}$
I	-0.5	2a	0.505	6.336	4.57	0.72	5.1
I	-1.5	2b, 3a	0.430	6.306	4.92	0.78	6.0
I	2.5	2c	0.299	6.233	5.79	0.93	8.5
II	-0.5	2d	0.441	5.711	7.63	1.34	9.6
III	0.5	SI6	3.84	5.588	5.63	1.01	2.4

The parameters are obtained from five sets of spectroscopy data in three circuits. The column ‘‘Figure’’ shows the corresponding figures. ‘‘SI’’ stands for Supplementary Information.

ground state. Theoretical fits to ω_{ij} were obtained by diagonalizing $\mathcal{H}_{\text{total}}$, treating Δ , ω_o , and g as fitting parameters. The obtained parameters are shown in Table I. The calculated transition frequencies ω_{ij}^{cal} are superimposed on the measured transmission spectra. As g increases, the anticrossing gap between the qubit and the oscillator frequencies at $\varepsilon \simeq \pm\omega_o$ becomes smaller and the signal from the $|1\rangle \rightarrow |3\rangle$ transition gradually transforms from a W shape to a Λ shape in the range $|\varepsilon| \lesssim \omega_o$. These features are seen in both the experimental data and the theoretical calculations, with good agreement between the data and the calculations. Note that ω_o depends on the qubit state and ε via L_{qc} , which results in the broad V shape seen in the spectra (see Supplementary Information, section S2).

To capture signals from more transitions, the transmission spectra in a wider ω_p range and a smaller ε range were measured, as shown in Fig. 3a for circuit I at $n_{\phi_q} = -1.5$. As we approach the symmetry point $\varepsilon = 0$, the signals from the $|0\rangle \rightarrow |2\rangle$ and $|1\rangle \rightarrow |3\rangle$ transitions disappear while signals from the $|0\rangle \rightarrow |3\rangle$ and $|1\rangle \rightarrow |2\rangle$ transitions appear near ω_{03}^{cal} and ω_{12}^{cal} . The appearance and disappearance of the signals are well explained by the transition matrix elements $T_{ij} = \langle i | (\hat{a} + \hat{a}^\dagger) | j \rangle$ shown in Fig. 3b: when $\varepsilon \rightarrow 0$, $|T_{02}| = |T_{13}| \rightarrow 0$ (forbidden transitions), while $|T_{03}|$ and $|T_{12}|$ are maximum (allowed transitions). As can be seen from the expression for T_{ij} , these features are directly related to the form of the energy eigenstates and can therefore serve as indicators of the symmetry properties of the energy

eigenstates, similarly to how atomic forbidden transitions are related to the symmetry of atomic wave functions. The weakness of the signals from the $|0\rangle \rightarrow |3\rangle$ and $|1\rangle \rightarrow |2\rangle$ transitions is probably due to dephasing caused by flux fluctuations. No signals from the $|0\rangle \rightarrow |3\rangle$ and $|1\rangle \rightarrow |2\rangle$ transitions were observed in circuit I at $n_{\phi_q} = 2.5$ and in circuit II. The broad dips at $\omega_p/2\pi = 6.2, 6.38,$ and 6.45 GHz are the result of a background frequency dependence of the transmission line's transmission amplitude, and these features can be ignored here. The feature at 6.2 GHz also contains a narrow signal from another qubit-oscillator circuit that is coupled to the transmission line (see Supplementary Information, section S3).

To conclude this analysis of the observed transmission spectra, the fact that the frequencies of the spectral lines and the points where they become forbidden follow, respectively, ω_{ij}^{cal} and $|T_{ij}|$ lends strong support to the conclusion that $\mathcal{H}_{\text{total}}$ accurately describes our circuits. Importantly, in circuits II and III, g is larger than both ω_o and Δ , emphasizing that the circuits are in the deep strong-coupling regime [$g \gtrsim \max(\omega_o, \sqrt{\Delta\omega_o}/2)$]²⁵. The fact that at $\varepsilon = 0$ the two forbidden transitions are located between the two allowed transitions is a further sign that $g > \omega_o/2$ (see Fig. 3c). In contrast, the highest coupling strengths achieved in previous experiments^{12,13} give $g/\omega_o = 0.12$ and 0.1 , respectively. From the spectrum in Fig. 3a, we find that $\omega_{01}(\varepsilon = 0)/\Delta = 0.13 \text{ GHz}/0.43 \text{ GHz} = 0.30$, meaning that the Lamb shift²⁶ is 70% of the bare qubit frequency. The same value (0.30) is obtained from theoretical calculations for $g/\omega_o = 0.78$.

Using our experimental results, we can make a statement regarding the A^2 term and the superradiance no-go theorem¹⁶ in our setup. A direct consequence of the no-go theorem is that, provided that the condition of the theorem ($C_{A2} > g/\Delta$) is satisfied, the system parameters will be renormalized such that the experimentally measured parameters will satisfy the inequality $2g/\sqrt{\Delta\omega_o} < 1$ (see Methods). However, in all five cases in our experiment, we find that $2g/\sqrt{\Delta\omega_o} > 1$, with the ratio on the left-hand side ranging from 2.4 to 9.6 (see Table I). These results demonstrate that the A^2 term in our setup does not satisfy the condition of the no-go theorem and therefore does not preclude a superradiant state. In fact, we expect that $C_{A2} \ll 1$ as shown in Methods.

The energy eigenstates of the qubit-oscillator system can be understood in the following way. In the absence of coupling, the energy eigenstates are product states where the oscillator is described by a Fock state $|n\rangle_o$ with n plasmons. Because of the coupling to the qubit,

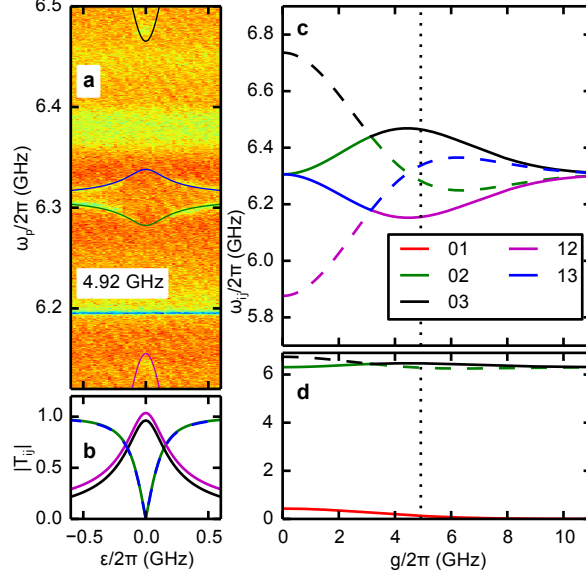


FIG. 3. **Selection rules and transmission spectrum around the symmetry point.** **a** Transmission spectrum for circuit I at $n_{\phi_q} = -1.5$ plotted as a function of flux bias ε . The transition frequencies ω_{ij}^{cal} superimposed on the experimental result in **a** and the matrix elements $|T_{ij}|$ plotted in **b** are calculated using the parameters shown in Table I, i.e. $\Delta/2\pi = 0.430$ GHz, $\omega_o/2\pi = 6.306$ GHz, and $g/2\pi = 4.92$ GHz. **c** The calculated transition frequencies around ω_o and **d** from the ground state are plotted as functions of g at $\varepsilon = 0$. The red, green, black, magenta, and blue lines in all four panels indicate the transitions $|0\rangle \rightarrow |1\rangle$, $|0\rangle \rightarrow |2\rangle$, $|0\rangle \rightarrow |3\rangle$, $|1\rangle \rightarrow |2\rangle$, and $|1\rangle \rightarrow |3\rangle$, respectively. Solid (dashed) lines in panels **c** and **d** indicate that the corresponding matrix elements T_{ij} are nonzero (zero). Allowed and forbidden transitions cross at $g/2\pi \simeq \omega_o/4\pi = 3.15$ GHz²⁵, where there is an energy-level crossing and the energy eigenstates $|2\rangle$ and $|3\rangle$ exchange their physical states. The black dotted line is at the coupling strength in circuit I at $n_{\phi_q} = -1.5$, $g/2\pi = 4.92$ GHz.

the state of the oscillator is displaced in one of two opposite directions depending on the persistent-current state of the qubit²⁵: $|L\rangle_q \otimes |n\rangle_o \rightarrow |L\rangle_q \otimes \hat{D}(-\alpha)|n\rangle_o$ and $|R\rangle_q \otimes |n\rangle_o \rightarrow |R\rangle_q \otimes \hat{D}(\alpha)|n\rangle_o$. Here, $\hat{D}(\alpha) = \exp(\alpha\hat{a}^\dagger - \alpha^*\hat{a})$ is the displacement operator, and α is the displacement. The amount of the displacement is approximately $\pm g/\omega_o$. As the energy eigenstates of an isolated qubit at $\varepsilon = 0$ are superpositions of the persistent-current states, $|g\rangle_q = (|L\rangle_q + |R\rangle_q)/\sqrt{2}$ and $|e\rangle_q = (|L\rangle_q - |R\rangle_q)/\sqrt{2}$, the energy eigenstates of the qubit-oscillator system at $\varepsilon = 0$ are well described by Schrödinger-cat-like entangled states between

TABLE II. **The energy eigenstates of the qubit-oscillator system.**

energy eigenbasis		qubit⟩ ⊗ oscillator⟩ basis	
$g < \frac{\omega_o}{2}$	$g > \frac{\omega_o}{2}$	arbitrary g	$g = 0$
0⟩	0⟩	$(L\rangle_q \otimes -\alpha\rangle_o + R\rangle_q \otimes \alpha\rangle_o)/\sqrt{2}$	$ g\rangle_q \otimes 0\rangle_o$
1⟩	1⟩	$(L\rangle_q \otimes -\alpha\rangle_o - R\rangle_q \otimes \alpha\rangle_o)/\sqrt{2}$	$ e\rangle_q \otimes 0\rangle_o$
2⟩	3⟩	$(L\rangle_q \otimes \hat{D}(-\alpha) 1\rangle_o + R\rangle_q \otimes \hat{D}(\alpha) 1\rangle_o)/\sqrt{2}$	$ g\rangle_q \otimes 1\rangle_o$
3⟩	2⟩	$(L\rangle_q \otimes \hat{D}(-\alpha) 1\rangle_o - R\rangle_q \otimes \hat{D}(\alpha) 1\rangle_o)/\sqrt{2}$	$ e\rangle_q \otimes 1\rangle_o$

The left two columns are written in the energy eigenbasis while the right two columns are written in the tensor product basis of qubit and oscillator states. At $g \simeq \omega_o/2$, there is an energy-level crossing and the energy eigenstates |2⟩ and |3⟩ exchange their physical states. |L⟩_q and |R⟩_q are the persistent-current states of the qubit, |g⟩_q and |e⟩_q are the energy eigenstates of the qubit, $|\pm\alpha\rangle_o = \hat{D}(\pm\alpha)|0\rangle_o$ are coherent states of the oscillator, $\hat{D}(\alpha)$ is a displacement operator, and $|n\rangle_o$ is a Fock state of the bare oscillator. At $g = 0$ and hence $\alpha = 0$, the energy eigenstates are product states, as shown in the right-most column. For arbitrary g , the energy eigenstates of the qubit-oscillator system are entangled states.

persistent-current states of the qubit and displaced Fock states of the oscillator $\hat{D}(\pm\alpha)|n\rangle_o$, as shown in Table II. Note that the displaced vacuum state $\hat{D}(\alpha)|0\rangle_o$ is the coherent state $|\alpha\rangle_o = \exp(-|\alpha|^2/2) \sum_{n=0}^{\infty} \alpha^n/\sqrt{n!}|n\rangle_o$. Although the above picture works best when $\omega_o \gg \Delta$, theoretical calculations show that it also gives a rather accurate description for circuit III (with $\omega_o/\Delta = 1.44$) (see Methods). The vanishing of the spectral lines corresponding to the $|0\rangle \rightarrow |2\rangle$ and $|1\rangle \rightarrow |3\rangle$ transitions at $\varepsilon = 0$ is a consequence of the symmetric form of the energy eigenstates. This symmetry is expected from the current-inversion symmetry in the Hamiltonian $\mathcal{H}_{\text{total}}$, and it supports the theoretical prediction that the energy eigenstates at that point are qubit-oscillator entangled states.

Using $\mathcal{H}_{\text{total}}$ and the parameters shown in Table I, we can calculate the qubit-oscillator ground-state entanglement \mathcal{E}_{gs} (see Supplementary Information, section S5). In all cases, $\mathcal{E}_{\text{gs}} \gtrsim 90\%$, and for circuit II in particular $\mathcal{E}_{\text{gs}} = 99.88\%$. In comparison, the ground-state

entanglement for the parameters of Refs. 12 and 13 is 6% and 4%, respectively. It should be noted here that in all five cases in our experiment there will be a significant population in the state $|1\rangle$ in thermal equilibrium, and the thermal-equilibrium qubit-oscillator entanglement will be reduced to below 8% for circuits I and II, and 25% for circuit III (see Supplementary Information, Table S1).

In conclusion, we have experimentally achieved deep-strong coupling between a superconducting flux qubit and an LC oscillator. Our results are consistent with the theoretical prediction that the energy eigenstates are Schrödinger-cat-like entangled states between persistent-current states of the qubit and displaced Fock states of the oscillator. We have also observed a huge Lamb shift, 70% of the bare qubit frequency. The tiny Lamb shift in natural atoms, which arises from weak vacuum fluctuations, was one of the earliest phenomena to stimulate the study of quantum electrodynamics. Now we can design artificial systems with light-matter interaction so strong that instead of speaking of vacuum fluctuations we speak of a strongly correlated light-matter ground state, defining a new state of matter and opening prospects for applications in quantum technologies.

Note added in proof: After acceptance of our paper, we became aware of a related manuscript (Ref. 27) taking a different approach to the same theme.

ACKNOWLEDGMENTS

We thank Kae Nemoto, Masao Hirokawa, Kunihiro Inomata, John W. Munro, Yuichiro Matsuzaki, Motoaki Bamba, and Norikazu Mizuochi for stimulating discussions. The authors are grateful to Mikio Fujiwara, Kentaro Wakui, Masahiro Takeoka, and Masahide Sasaki for their continued support through all the stages of this research. We thank Junichi Komuro, Shinya Inoue, and Etsuro Sasaki for assistance with experimental setup.

We also thank Sander Weinreb for their support by providing excellent cryoamplifiers, and Noriyoshi Matsuura and Yoshitada Kato for their cordial support in the startup phase of this research. Some of our calculations were performed using the QuTiP simulation package²⁸.

This work was supported in part by the Scientific Research (S) Grant No. JP25220601 by the Japanese Society for the Promotion of Science (JSPS).

AUTHOR CONTRIBUTIONS

All authors contributed extensively to the work presented in this paper. F. Y., T. F., K. S. carried out measurements and data analysis on the coupled flux qubit - LC-oscillator circuits. F. Y., T. F. designed and F. Y., T. F., K. K. fabricated the flux-qubit and associated devices. T. F., F. Y., K. K., S. S., and K. S. designed and developed the measurement system. S. A. provided theoretical support and analysis. F. Y., T. F., S. A., and K. S. wrote the manuscript, with feedback from all authors. K. S. designed and supervised the project.

METHODS

Laser microscope image. The laser microscope image in Fig. 1b was obtained by Keyence VK-9710 Color 3D Laser Scanning Microscope. The magnification of the objective lens is 10. The application “VK Viewer” was used for image acquisition.

Scanning electron microscope image. The scanning electron microscope image in Fig. 1c was obtained by JEOL JIB-4601F. The acceleration voltage was 10 kV, the magnification was 6500, and the working distance was 8.7 mm.

Nonlinearity of M and the A^2 term of the total Hamiltonian. We now consider the nonlinearity of the mutual inductance M between the flux qubit and the LC oscillator. As discussed in the Supplementary Information, M is almost the same as L_c in Fig. 1a, which depends on the current flowing through the Josephson junction I_b as $L_c(I_b) = \Phi_0 / (2\pi \sqrt{(a_c I_c)^2 - I_b^2})$, where $a_c I_c \equiv I_{cM}$ is the critical current of the Josephson junction. We thus assume that M can similarly be written as

$$M(I_b) = \frac{\Phi_0}{2\pi \sqrt{I_{cM}^2 - I_b^2}}. \quad (2)$$

The nonlinearity of $M(I_b)$ up to second order in δI_b can be written as

$$\begin{aligned} M(I_b + \delta I_b) &= M(I_b) + \delta I_b \frac{\partial M(I_b)}{\partial I_b} + \frac{\delta I_b^2}{2} \frac{\partial^2 M(I_b)}{\partial I_b^2} \\ &= M(I_b) \left(1 + \frac{I_b \delta I_b}{I_{cM}^2 - I_b^2} + \frac{I_{cM}^2 + 2I_b^2}{2(I_{cM}^2 - I_b^2)^2} \delta I_b^2 \right). \end{aligned} \quad (3)$$

The coupling Hamiltonian can be written as $\mathcal{H}_c = M(\hat{I}_q + \hat{I}_o)\hat{I}_q\hat{I}_o = M(\hat{I}_q + \hat{I}_o)I_p\sigma_z I_{\text{zpf}}(\hat{a} + \hat{a}^\dagger)$, where $\hat{I}_q = I_p\sigma_z$ is the persistent-current operator of the qubit, $\hat{I}_o = I_{\text{zpf}}(\hat{a} + \hat{a}^\dagger)$ is the current operator of the oscillator, and the current $\hat{I}_q + \hat{I}_o$ flows through the mutual inductance. Typically, $I_p \gg I_{\text{zpf}}$. Taking into account the nonlinearity of $M(\hat{I}_q + \hat{I}_o)$, the coupling Hamiltonian is written as

$$\begin{aligned}
\mathcal{H}_c &= M(\hat{I}_q + \hat{I}_o)\hat{I}_q\hat{I}_o \\
&= M(\hat{I}_q) \left(1 + \frac{\hat{I}_q\hat{I}_o}{I_{\text{cM}}^2 - \hat{I}_q^2} + \frac{I_{\text{cM}}^2 + 2\hat{I}_q^2}{2(I_{\text{cM}}^2 - \hat{I}_q^2)^2}\hat{I}_o^2 \right) \hat{I}_q\hat{I}_o \\
&= M(I_p) \left[I_p I_{\text{zpf}} \sigma_z (\hat{a} + \hat{a}^\dagger) + \frac{I_p^2 I_{\text{zpf}}^2}{I_{\text{cM}}^2 - I_p^2} (\hat{a} + \hat{a}^\dagger)^2 + \frac{(I_{\text{cM}}^2 + 2I_p^2) I_p I_{\text{zpf}}^3}{2(I_{\text{cM}}^2 - I_p^2)^2} \sigma_z (\hat{a} + \hat{a}^\dagger)^3 \right] \\
&= \hbar g [\sigma_z (\hat{a} + \hat{a}^\dagger) + C_{\text{A2}} (\hat{a} + \hat{a}^\dagger)^2 + C_{\text{A3}} \sigma_z (\hat{a} + \hat{a}^\dagger)^3], \tag{4}
\end{aligned}$$

where

$$\hbar g = M(I_p) I_p I_{\text{zpf}}, \tag{5}$$

$$C_{\text{A2}} = \frac{I_p I_{\text{zpf}}}{I_{\text{cM}}^2 - I_p^2}, \tag{6}$$

and

$$C_{\text{A3}} = \frac{(I_{\text{cM}}^2 + 2I_p^2) I_{\text{zpf}}^2}{2(I_{\text{cM}}^2 - I_p^2)^2}. \tag{7}$$

Here, we considered terms up to second order in I_{zpf}/I_p . We find that $1 \gg C_{\text{A2}} \gg C_{\text{A3}}$ considering the following relation, $I_{\text{cM}} (= a_c I_c) > I_p (\lesssim a_3 I_c) \gg I_{\text{zpf}} (\ll I_c)$, where $a_c \gtrsim 1$ (see Supplementary Material), $0.4 \lesssim a_3 \lesssim 0.8$, I_c is several hundred nano amperes, and I_{zpf} is several ten nano amperes. Since the term C_{A3} is very small, we ignore the third term in Eq. (4).

The total Hamiltonian of the circuit considering the nonlinearity of M up to first order in I_{zpf}/I_p is given by

$$\mathcal{H}_{\text{total}} = -\frac{\hbar}{2}(\Delta\sigma_x + \varepsilon\sigma_z) + \hbar\omega_o \left(\hat{a}^\dagger\hat{a} + \frac{1}{2}\right) + \hbar g\sigma_z(\hat{a} + \hat{a}^\dagger) + C_{A2}\hbar g(\hat{a} + \hat{a}^\dagger)^2, \quad (8)$$

where the first term is the Hamiltonian of the flux qubit, the second term is the Hamiltonian of the LC oscillator, and the third term is the coupling Hamiltonian. The fourth term proportional to $(\hat{a} + \hat{a}^\dagger)^2$ is known as the A^2 term in atomic physics. This term can be eliminated by a variable transformation as

$$\begin{aligned} \mathcal{H}_{\text{total}} &= -\frac{\hbar}{2}(\Delta\sigma_x + \varepsilon\sigma_z) + \hbar\omega_o \left(\hat{a}^\dagger\hat{a} + \frac{1}{2}\right) + C_{A2}\hbar g(\hat{a} + \hat{a}^\dagger)^2 + \hbar g\sigma_z(\hat{a} + \hat{a}^\dagger) \\ &= -\frac{\hbar}{2}(\Delta\sigma_x + \varepsilon\sigma_z) + \left(\frac{\hbar\omega_o}{4} + C_{A2}\hbar g\right) (\hat{a} + \hat{a}^\dagger)^2 - \frac{\hbar\omega_o}{4}(\hat{a} - \hat{a}^\dagger)^2 + \hbar g\sigma_z(\hat{a} + \hat{a}^\dagger) \\ &= -\frac{\hbar}{2}(\Delta\sigma_x + \varepsilon\sigma_z) + \frac{\hbar\omega'_o}{4}(\hat{b} + \hat{b}^\dagger)^2 - \frac{\hbar\omega'_o}{4}(\hat{b} - \hat{b}^\dagger)^2 + \hbar g'\sigma_z(\hat{b} + \hat{b}^\dagger) \\ &= -\frac{\hbar}{2}(\Delta\sigma_x + \varepsilon\sigma_z) + \hbar\omega'_o\left(\hat{b}^\dagger\hat{b} + \frac{1}{2}\right) + \hbar g'\sigma_z(\hat{b} + \hat{b}^\dagger), \end{aligned} \quad (9)$$

where

$$\omega'_o = \sqrt{\omega_o^2 + 4C_{A2}g\omega_o}, \quad (10)$$

$$g' = \sqrt{\frac{\omega_o}{\omega'_o}}g, \quad (11)$$

and the new field operators,

$$\hat{b} + \hat{b}^\dagger = \sqrt{\frac{\omega'_o}{\omega_o}}(\hat{a} + \hat{a}^\dagger) \quad (12)$$

and

$$\hat{b} - \hat{b}^\dagger = \sqrt{\frac{\omega_o}{\omega'_o}}(\hat{a} - \hat{a}^\dagger), \quad (13)$$

are used. The form of the Hamiltonian in Eq. (9) is exactly the same as the one where the coupling term is linear in $(\hat{a} + \hat{a}^\dagger)$, which is given by

$$\mathcal{H}_{\text{total}}^{\text{linear}} = -\frac{\hbar}{2}(\Delta\sigma_x + \varepsilon\sigma_z) + \hbar\omega_o\left(\hat{a}^\dagger\hat{a} + \frac{1}{2}\right) + \hbar g\sigma_z(\hat{a} + \hat{a}^\dagger). \quad (14)$$

Note that the transformation described by Eqs. (12) and (13) is a Hopfield-Bogoliubov transformation²⁹. It guarantees that $[\hat{b}, \hat{b}^\dagger] = [\hat{a}, \hat{a}^\dagger] = 1$. In other words, both the \hat{a} operators and the \hat{b} operators obey the harmonic oscillator commutation relations. The two sets of operators are related to each other by quadrature squeezing operations. The most natural choice among these two and all other quadrature-squeezed variants is the one that leads to the standard form of the harmonic oscillator Hamiltonian, usually expressed as $\hbar\omega_o\hat{a}^\dagger\hat{a}$. As such, the \hat{b} operators are the most natural oscillator operators for our circuits. The \hat{a} operators were defined based on an incomplete description of the circuit, considering the properties of the LC circuit and ignoring the qubit and coupler parts of the circuit. In particular, the A^2 term in our circuits describes an additional contribution to the inductive energy of the oscillator that arises in the presence of the qubit and coupler circuits. Similarly, the expression given in the main text for the current zero-point fluctuations must be modified in order to correctly describe the fluctuations in the full circuit.

Condition for superradiant phase transition. In cases where one expects a sharp transition from a normal to a superradiant state, e.g. when $\Delta \gg \omega_o$ or when the single qubit is replaced by a large ensemble of N qubits (and g is defined to include the ensemble enhancement factor \sqrt{N}), the phase transition condition (without the A^2 term) is:

$$4g^2 = \Delta \times \omega_o. \quad (15)$$

After taking into account the renormalization of ω_o and g caused by the A^2 term as described above, the condition for the phase transition becomes

$$4g^2 \sqrt{\frac{\omega_o}{\omega_o + 4C_{A2}g}} = \Delta \times \omega_o \times \sqrt{\frac{\omega_o + 4C_{A2}g}{\omega_o}}, \quad (16)$$

or in other words

$$4g^2 = \Delta \times (\omega_o + 4C_{A2}g). \quad (17)$$

If the parameters are constrained to satisfy the relation $C_{A2} > g/\Delta$, the right-hand side increases whenever we increase the left-hand side, and no matter how large g becomes it will never be strong enough to satisfy the phase transition condition. This can indeed be the case with atomic qubits, and it leads to the no-go theorem in those systems¹⁶.

Fidelities of qubit-oscillator entangled states for circuit III. The fidelity between two pure states $|\phi\rangle$ and $|\psi\rangle$ is given by $F(|\phi\rangle, |\psi\rangle) = |\langle\phi|\psi\rangle|^2$. For circuit III, the fidelities between the four lowest energy eigenstates given in Table II $|i_{\text{III}}\rangle$ and the corresponding exact

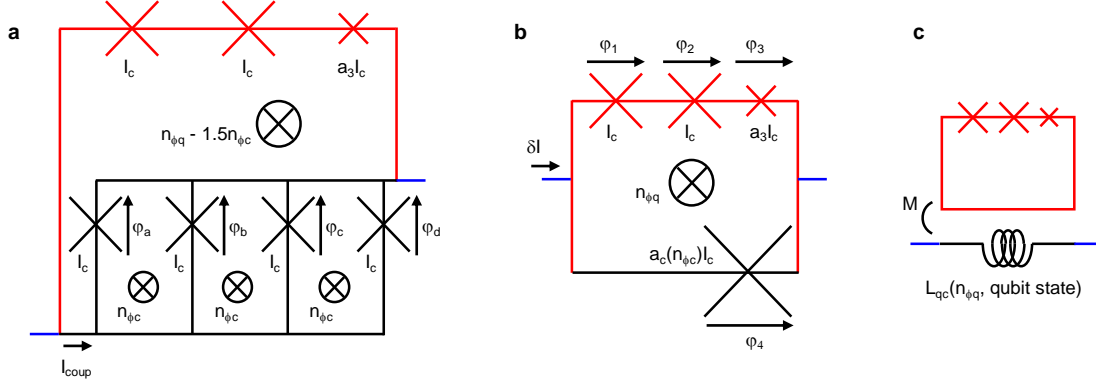


FIG. S1. **Circuit diagrams of the flux qubit and coupler.** **a**, The qubit (red and black) consists of three Josephson junctions in the upper branch (red) and the coupler (black), which is four parallel Josephson junctions. **b**, The coupler junctions are simplified to a single effective Josephson junction. **c**, The equivalent circuit of **b**, now consisting of the mutual inductance M and the inductance across the qubit and the coupler L_{qc} , which depends on both the flux bias and the qubit state.

energy eigenstates of $\mathcal{H}_{\text{total}}$ $|i_{\text{exact}}\rangle$ ($i = 0, 1, 2, 3$) are calculated to be $F(|0_{\text{TII}}\rangle, |0_{\text{exact}}\rangle) = 0.981$, $F(|1_{\text{TII}}\rangle, |1_{\text{exact}}\rangle) = 0.985$, $F(|2_{\text{TII}}\rangle, |2_{\text{exact}}\rangle) = 0.975$, and $F(|3_{\text{TII}}\rangle, |3_{\text{exact}}\rangle) = 0.967$. All the other data sets give significantly higher fidelities. In particular, for circuit II $F(|0_{\text{TII}}\rangle, |0_{\text{exact}}\rangle) = 0.99994$.

SUPPLEMENTARY INFORMATION

S1. FLUX BIAS DEPENDENCE OF THE COUPLER'S CRITICAL CURRENT

The circuit diagram of the coupler in circuit I is shown as the black part of the circuit in Fig. S1a. Here, n_{ϕ_c} is the normalized flux bias in units of the superconducting flux quantum $\Phi_0 = h/2e$ through each coupler loop defined by two neighboring parallel junctions. The critical currents of the two large junctions of the flux qubit and the four junctions of the coupler are all approximately equal, with the value I_c . The current through the coupler I_{coup} is the sum of the currents across the four Josephson junctions: $I_{\text{coup}} = I_c(\sin \varphi_a + \sin \varphi_b + \sin \varphi_c + \sin \varphi_d)$, where φ_i ($i = a, b, c, d$) is the phase across junction i . Considering the fluxoid quantization of each loop, the phases can be written using φ_a and n_{ϕ_c} as

$$\varphi_b = \varphi_a + 2\pi n_{\phi c}, \quad (\text{S18})$$

$$\varphi_c = \varphi_a + 4\pi n_{\phi c}, \quad (\text{S19})$$

and

$$\varphi_d = \varphi_a + 6\pi n_{\phi c}. \quad (\text{S20})$$

Here, we ignore the sum of the kinetic and geometric inductances of the superconducting lead, which is at least an order of magnitude smaller than those of the Josephson junctions. Using Eqs. (S18)–(S20), I_{coup} can be written as

$$\begin{aligned} I_{\text{coup}} &= I_c [\sin \varphi_a + \sin(\varphi_a + 2\pi n_{\phi c}) + \sin(\varphi_a + 4\pi n_{\phi c}) + \sin(\varphi_a + 6\pi n_{\phi c})] \\ &= 2I_c [\sin(\varphi_a + \pi n_{\phi c}) \cos(\pi n_{\phi c}) + \sin(\varphi_a + 5\pi n_{\phi c}) \cos(\pi n_{\phi c})] \\ &= 4I_c \sin(\varphi_a + 3\pi n_{\phi c}) \cos(2\pi n_{\phi c}) \cos(\pi n_{\phi c}). \end{aligned} \quad (\text{S21})$$

Thus, the critical current of the coupler $I_{c(\text{coup})}$ can be described by the ratio

$$a_c(n_{\phi c}) = \frac{I_{c(\text{coup})}}{I_c} = 4 \cos(2\pi n_{\phi c}) \cos(\pi n_{\phi c}). \quad (\text{S22})$$

Now, the coupler junctions in Fig. S1a can be replaced by a single effective Josephson junction whose critical current is $a_c(n_{\phi c})I_c$ as shown in Fig. S1b. Circuit II is almost the same as circuit I except that its coupler consists of two Josephson junctions of critical current I_c , forming a superconducting quantum interference device (SQUID). The critical-current ratio of the SQUID is described by

$$a_{c\text{II}}(n_{\phi c\text{II}}) = 2 \cos(\pi n_{\phi c\text{II}}), \quad (\text{S23})$$

where $n_{\phi c\text{II}}$ is the normalized flux bias through the SQUID loop. Thus, the circuit diagram of the flux qubit in circuit II is also described by Fig. S1b.

S2. ESTIMATION OF L_{qc} AND M

The circuit in Fig. S1b should be simplified to the one in Fig. S1c to estimate L_{qc} and M as functions of the bias current δI coming from the current in the LC oscillator and normalized flux bias through the qubit loop $n_{\phi\text{q}}$ in units of Φ_0 . The total Josephson energy of the circuit is given by

$$E_{\text{J}}^{\text{total}} = -E_{\text{J}} [\cos \varphi_1 + \cos \varphi_2 + a_3 \cos \varphi_3 + a_c \cos(-\varphi_{\text{u}} + 2\pi n_{\phi\text{q}})] - \frac{\delta I \Phi_0}{2\pi} \varphi_{\text{x}}, \quad (\text{S24})$$

where $E_{\text{J}} = \Phi_0 I_c / 2\pi$, φ_i ($i = 1, 2, 3$) is the phase difference across the i th junction, a_3 and a_c are the critical current ratios of the third and the coupler junctions, $\varphi_{\text{u}} = \varphi_1 + \varphi_2 + \varphi_3$ is the phase difference across the upper branch of the qubit loop, and $\varphi_{\text{x}} = (\varphi_{\text{u}} + \pi n_{\phi\text{q}})$ is the average phase difference across the upper and lower branches of the qubit loop. The last term is the energy of the bias current source.

At $n_{\phi\text{q}} \sim 0.5$, $E_{\text{J}}^{\text{total}}$ has two local minima in the three-dimensional parameter space spanned by φ_1 , φ_2 , and φ_3 . The localized state at each minimum corresponds to one of the two persistent-current states of the flux qubit, $|\text{L}\rangle_{\text{q}}$ and $|\text{R}\rangle_{\text{q}}$. For simplicity, we use the sets of phases $\{\varphi_i^{|\text{L}\rangle}\}$ and $\{\varphi_i^{|\text{R}\rangle}\}$ at the minima of $E_{\text{J}}^{\text{total}}$ as the values of the different phases for $|\text{L}\rangle_{\text{q}}$ and $|\text{R}\rangle_{\text{q}}$. Figure S2a shows the $n_{\phi\text{q}}$ dependence of different phases corresponding to $|\text{L}\rangle_{\text{q}}$ and $|\text{R}\rangle_{\text{q}}$. In the calculation, the parameters $I_c = 460$ nA and $a_3 = 0.705$, which are estimated from other samples fabricated simultaneously in the same fabrication process, are used. We also assume that the global magnetic field simultaneously provides flux bias through the loops of the qubit and the coupler according to their area ratio as $n_{\phi\text{q}} : n_{\phi\text{c}} = 24 : 1$.

The qubit-state-dependent inductance across the qubit and coupler $L_{\text{qc}}^{|\text{L(R)}\rangle}$ is calculated considering the Josephson inductances, $L_{\text{J1}}^{|\text{L(R)}\rangle} = \Phi_0 / (2\pi I_c \cos \varphi_1^{|\text{L(R)}\rangle})$, $L_{\text{J2}}^{|\text{L(R)}\rangle} = \Phi_0 / (2\pi I_c \cos \varphi_2^{|\text{L(R)}\rangle})$, $L_{\text{J3}}^{|\text{L(R)}\rangle} = \Phi_0 / (2\pi a_3 I_c \cos \varphi_3^{|\text{L(R)}\rangle})$, and $L_{\text{J4}}^{|\text{L(R)}\rangle} = \Phi_0 / (2\pi a_c I_c \cos \varphi_4^{|\text{L(R)}\rangle})$, as

$$L_{\text{qc}}^{|\text{L(R)}\rangle} = \frac{L_{\text{J4}}^{|\text{L(R)}\rangle} (L_{\text{J1}}^{|\text{L(R)}\rangle} + L_{\text{J2}}^{|\text{L(R)}\rangle} + L_{\text{J3}}^{|\text{L(R)}\rangle})}{L_{\text{J1}}^{|\text{L(R)}\rangle} + L_{\text{J2}}^{|\text{L(R)}\rangle} + L_{\text{J3}}^{|\text{L(R)}\rangle} + L_{\text{J4}}^{|\text{L(R)}\rangle}}. \quad (\text{S25})$$

Figure S2d shows the flux-bias dependence of $L_{\text{qc}}^{|\text{L}\rangle}$ and $L_{\text{qc}}^{|\text{R}\rangle}$, which can be approximately described as $L_{\text{qc}}^{|\text{L}\rangle} = L_{\text{qc0}} + D_{\text{L}}^{|\text{L}\rangle} (n_{\phi\text{q}} - 0.5)$ and $L_{\text{qc}}^{|\text{R}\rangle} = L_{\text{qc0}} - D_{\text{L}}^{|\text{R}\rangle} (n_{\phi\text{q}} - 0.5)$ ($D_{\text{L}}^{|\text{L}\rangle} \sim D_{\text{L}}^{|\text{R}\rangle} < 0$), respectively. The small asymmetry between $L_{\text{qc}}^{|\text{L}\rangle}$ and $L_{\text{qc}}^{|\text{R}\rangle}$ is due to the flux-bias dependence

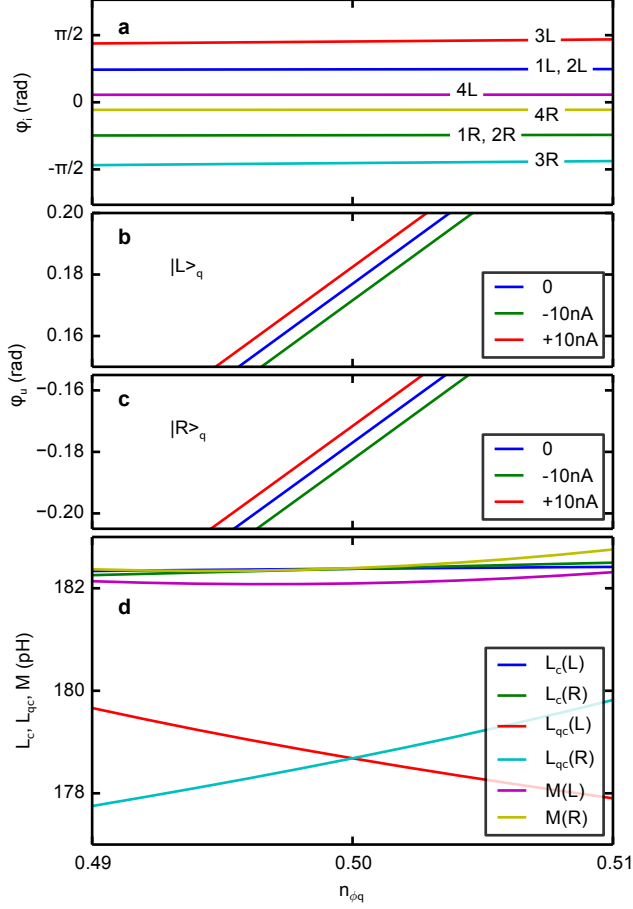


FIG. S2. **Flux bias dependence of phases and inductances.** **a**, The flux bias dependence of the phase across the different Josephson junctions in Fig. S1b when the qubit state is $|L\rangle_q$ and $|R\rangle_q$. **b** (**c**), The flux bias dependence of the phase across the upper branch of the qubit loop φ_u at three different current bias values, $\delta I = 0, \pm 10$ nA, when the qubit state is $|L\rangle_q$ ($|R\rangle_q$). **d**, The flux bias dependence of the coupler inductance L_c , the mutual inductance M , and the inductance across the qubit and the coupler L_{qc} when the qubit state is $|L\rangle_q$ and $|R\rangle_q$.

of $a_c(n_{\phi_c})$. Note that at $n_{\phi_q} = 0.5$, $L_{qc}^{(L)} = L_{qc}^{(R)} = L_{qc0}$. The inductances of the coupler junction, $L_c^{(L(R))} = L_{J4}^{(L(R))}$ are also plotted in Fig. S2d, and are slightly larger than $L_{qc}^{(L(R))}$.

It is more convenient to describe the qubit-state-dependent inductance using the energy eigenstates of the qubit, $|g\rangle_q$ and $|e\rangle_q$, as

$$\begin{aligned}
L_{\text{qc}} &= \frac{1}{2}(L_{\text{qc}}^{|\text{g}\rangle} + L_{\text{qc}}^{|\text{e}\rangle}) + \frac{1}{2}(L_{\text{qc}}^{|\text{g}\rangle} - L_{\text{qc}}^{|\text{e}\rangle})\sigma_z^{\text{eig}} \\
&= \frac{1}{2}(L_{\text{qc}}^{|\text{g}\rangle} + L_{\text{qc}}^{|\text{e}\rangle}) + \frac{1}{2}(L_{\text{qc}}^{|\text{g}\rangle} - L_{\text{qc}}^{|\text{e}\rangle})(\cos\theta\sigma_z + \sin\theta\sigma_x),
\end{aligned} \tag{S26}$$

where σ_z^{eig} is Pauli matrix in the energy eigenbasis, $\sigma_{x,z}$ are Pauli matrices in the persistent-current basis, θ is defined as $\cos\theta = \varepsilon/\sqrt{\Delta^2 + \varepsilon^2}$, and $L_{\text{qc}}^{|\text{g(e)}\rangle}$ is the inductance across the qubit and the coupler when the qubit state is $|\text{g(e)}\rangle_{\text{q}}$. The relation between the persistent-current states and the energy eigenstates of the qubit is written as

$$\begin{pmatrix} |\text{g}\rangle_{\text{q}} \\ |\text{e}\rangle_{\text{q}} \end{pmatrix} = \begin{pmatrix} \cos\frac{\theta}{2} & \sin\frac{\theta}{2} \\ \sin\frac{\theta}{2} & -\cos\frac{\theta}{2} \end{pmatrix} \begin{pmatrix} |\text{L}\rangle_{\text{q}} \\ |\text{R}\rangle_{\text{q}} \end{pmatrix}. \tag{S27}$$

Thus $L_{\text{qc}}^{|\text{L(R)}\rangle}$ can be transformed to $L_{\text{qc}}^{|\text{g(e)}\rangle}$ as

$$\begin{pmatrix} L_{\text{qc}}^{|\text{g}\rangle} \\ L_{\text{qc}}^{|\text{e}\rangle} \end{pmatrix} = \begin{pmatrix} \cos^2\frac{\theta}{2} & \sin^2\frac{\theta}{2} \\ \sin^2\frac{\theta}{2} & \cos^2\frac{\theta}{2} \end{pmatrix} \begin{pmatrix} L_{\text{qc}}^{|\text{L}\rangle} \\ L_{\text{qc}}^{|\text{R}\rangle} \end{pmatrix}. \tag{S28}$$

$L_{\text{qc}}^{|\text{L(R)}\rangle}$ and $L_{\text{qc}}^{|\text{g(e)}\rangle}$ are shown in Fig. S3 as functions of the energy bias ε : $L_{\text{qc}}^{|\text{L}\rangle}$ and $L_{\text{qc}}^{|\text{R}\rangle}$ are straight lines, while $L_{\text{qc}}^{|\text{g}\rangle}$ and $L_{\text{qc}}^{|\text{e}\rangle}$ are Λ -shaped and V-shaped, respectively. Note that the resonance frequency of the LC oscillator $\omega_o = \frac{1}{\sqrt{(L_0 + L_{\text{qc}})C}}$ also depends on the qubit state and the flux bias via L_{qc} except at $\varepsilon = 0$. At sufficiently low temperatures, the qubit is in the ground state, and ω_o as a function of ε is V shaped.

The mutual inductance between the qubit loop and the LC oscillator M can be calculated as $M = \Phi_0|\delta n_{\phi\text{q}}/\delta I|$, where $(\partial\varphi_{\text{u}}/\partial n_{\phi\text{q}})\delta n_{\phi\text{q}} = [\varphi_{\text{u}}(\delta I) - \varphi_{\text{u}}(-\delta I)]/2$. The phase φ_{u} for $|\text{L}\rangle$ ($|\text{R}\rangle$) as a function of $n_{\phi\text{q}}$ at $\delta I = \pm 10$ nA is shifted from that at $\delta I = 0$ as shown in Fig. S2b (c). From the shifts, M is obtained as shown in Fig. S2d. M is found to be very close to the coupler inductance L_c . The flux bias dependence of $a_c(n_{\phi\text{c}})$ causes a small difference in M between two cases of $|\text{L}\rangle_{\text{q}}$ and $|\text{R}\rangle_{\text{q}}$, which is less than 1 % and we ignore it in the analysis in the main text and the consideration of the nonlinearity of M in Methods.

S3. MEASUREMENT SETUP

On each of two sample chips that we prepared, there are four qubit-oscillator circuits coupled to a single coplanar transmission line. In order to make them easily identifiable,

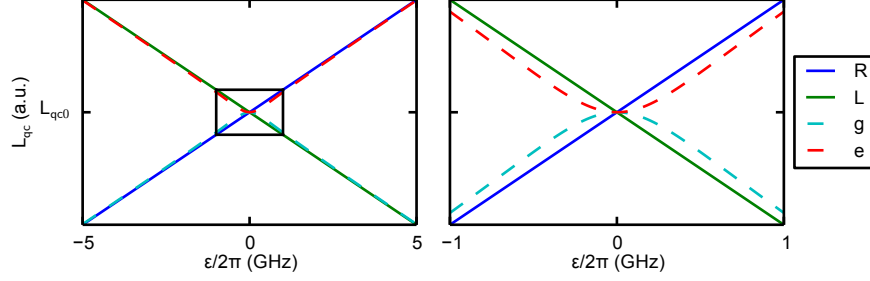


FIG. S3. **Flux-bias and qubit-state dependences of L_{qc} .** The right panel is the magnification of the rectangle part of the left panel. The blue and green solid lines and the red and cyan dashed lines correspond to $L_{qc}^{(R)}$, $L_{qc}^{(L)}$, $L_{qc}^{(g)}$, and $L_{qc}^{(e)}$, respectively.

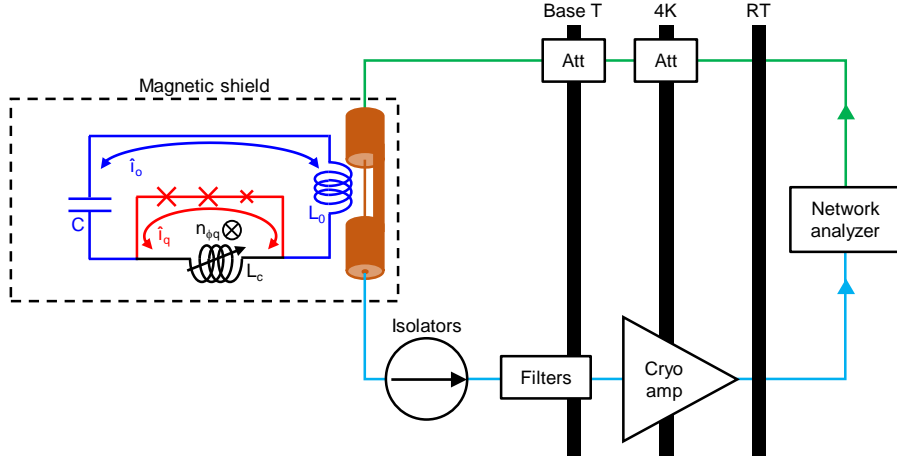


FIG. S4. **Measurement setup.** The sample of flux qubit coupled to the LC oscillator is cooled down in a dilution refrigerator and measured using a network analyzer. For the sample details, see Fig. 1 in the main text. The green and cyan lines are the signal input and output lines, respectively.

we designed the four oscillators to have different resonant frequencies and the four qubits to have different areas. The energy spectroscopy of the qubit-oscillator circuit is performed via the coplanar transmission line, which is inductively coupled to the LC oscillator, as shown in Fig. S4. The probe microwave signal is continuous, sent from a network analyzer (Agilent N5234A), and attenuated in the signal input line before arriving at the sample, which is placed in a magnetic shield. The transmitted signal from the sample is amplified (by Caltech cryogenic LNA model CITCRYO1-12A) and measured by the network analyzer. When the frequency of the probe signal ω_p matches the frequency of a transition between

two energy levels, the transmission amplitude decreases, provided that the transition matrix element is not zero. The input power is kept as low as possible to avoid cascade transitions, such as the transition $|i\rangle \rightarrow |j\rangle$ followed by $|j\rangle \rightarrow |k\rangle$ when $\omega_p \simeq \omega_{ij} \simeq \omega_{jk}$. The samples are measured in a dilution refrigerator with a nominal base temperature of 10 mK. From the depth ratio of the signals from the $|0\rangle \rightarrow |2\rangle$ and $|1\rangle \rightarrow |3\rangle$ transitions shown in Fig. 3a in the main text, which is directly related to the population ratio of the states $|0\rangle$ and $|1\rangle$, the temperature of circuit I at $n_\phi = -1.5$ can be estimated to be approximately 45 mK. In Figs. 2 and 3 in the main text and Figs. S5 and S6, the transmission spectrum $S_{21}(\omega_p)$ is measured at each flux bias ε , and $|S_{21}(\omega_p, \varepsilon)|$ is shown.

S4. WIGNER FUNCTION OF THE REDUCED DENSITY OPERATORS OF THE OSCILLATOR

Fig. S7 shows the Wigner functions⁶, $W(\alpha, \rho) = (1/\pi^2) \int \exp(\eta^* \alpha - \eta \alpha^*) \text{tr}[\rho \exp(\eta \hat{a}^\dagger - \eta^* \hat{a})] d^2 \eta$, of the reduced density operators of the oscillator $\text{tr}_q(|0\rangle\langle 0|)$ and $\text{tr}_q(|2\rangle\langle 2|)$ in the case of circuit II, where the states $|0\rangle$ and $|2\rangle$ are calculated from $\mathcal{H}_{\text{total}}$ using the parameters in Table I in the main text, and tr_q is the partial trace over qubit states. The states $\text{tr}_q(|0\rangle\langle 0|)$ and $\text{tr}_q(|2\rangle\langle 2|)$ are well described by mixtures of the two coherent states $|\pm \alpha\rangle$ and the two displaced Fock states $\hat{D}(\pm \alpha)|1\rangle$ separated from each other by $2\alpha = 2.67$, where the overlap between the two coherent states is $\langle -\alpha | \alpha \rangle = 0.028$.

S5. EVALUATION OF QUBIT-OSCILLATOR ENTANGLEMENT

The qubit-oscillator entanglement in the ground state can be evaluated as the (base-2) von Neumann entropy of the qubit³⁰:

$$\mathcal{E}_{\text{gs}} = -\text{Tr}\{\rho_q \log_2 \rho_q\}, \quad (\text{S29})$$

where ρ_q is the qubit's reduced density matrix obtained by tracing out the oscillator degree of freedom from the qubit-oscillator ground state. Figure S8 shows \mathcal{E}_{gs} as a function of α , where α is g/ω_o . We can see from this figure that \mathcal{E}_{gs} increases and approaches 1 as α increases above 1.

The entanglement for the thermal-equilibrium state can be evaluated as twice the Nega-

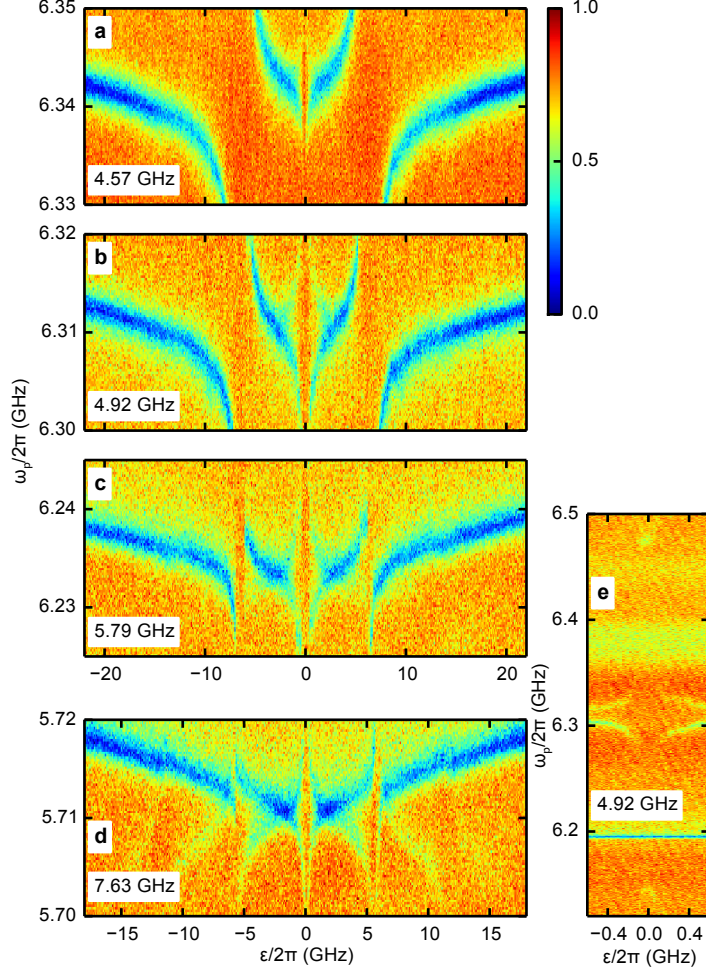


FIG. S5. **Transmission spectra for circuit I and II without the fitting curves.** The normalized amplitude of the transmission spectra as functions of flux bias ϵ . These spectra are the same as Fig. 2a–d and 3a in the main text without calculated transition frequencies ω_{ij}^{cal} . As summarized in Table I in the main text, panel **a** shows data from circuit I at $n_{\phi q} = -0.5$, panels **b** and **e** show data from circuit I at $n_{\phi q} = -1.5$, panel **c** shows data from circuit I at $n_{\phi q} = 2.5$, and panel **d** shows data from circuit II at $n_{\phi q} = -0.5$. The values of $g/2\pi$ are written in the panels.

tivity³⁰ (which is one of the mixed-state entanglement measures used in the literature):

$$\mathcal{E}_{\text{te}} = 2\mathcal{N} = 2 \sum_{\lambda < 0} |\lambda|, \quad (\text{S30})$$

where λ are eigenvalues of ρ^Γ , ρ is the thermal-equilibrium density matrix of the qubit-oscillator system, the superscript Γ indicates taking the partial transpose with respect to the degree of freedom of either the qubit or the oscillator, and the sum is taken over the negative eigenvalues only. The factor 2 is used to make \mathcal{E}_{te} range from 0 to 1.

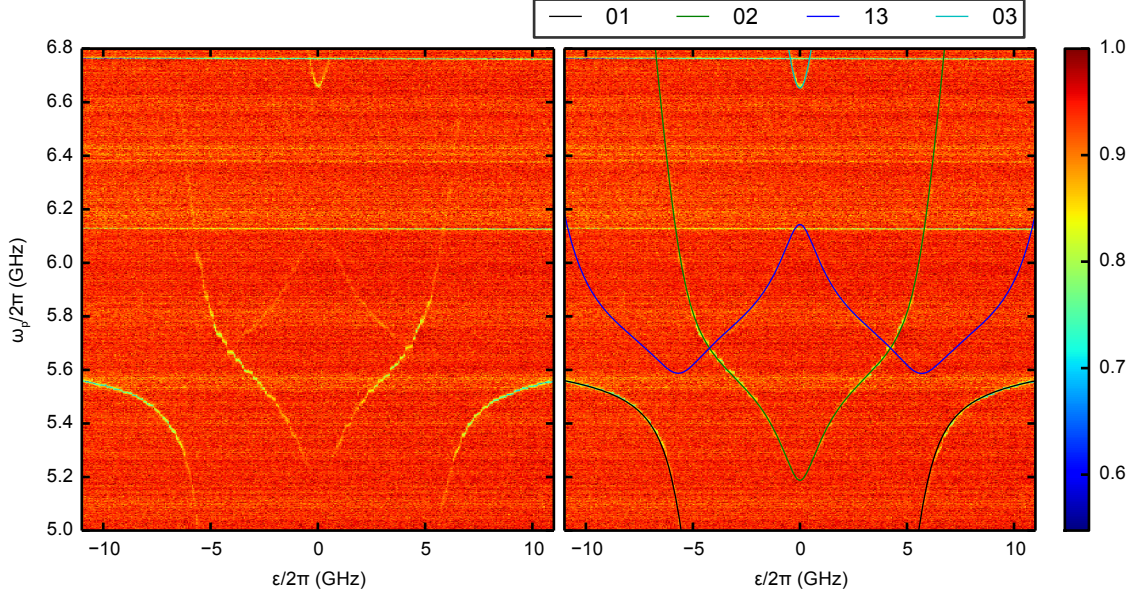


FIG. S6. **Transmission spectra for circuit III.** The normalized amplitude of the transmission spectra (with calculated transition frequencies ω_{ij}^{cal} in the right panel). The black, green, blue, and cyan lines indicate the transitions $|0\rangle \rightarrow |1\rangle$, $|0\rangle \rightarrow |2\rangle$, $|1\rangle \rightarrow |3\rangle$, and $|0\rangle \rightarrow |3\rangle$, respectively. The horizontal signals at 6.12 GHz and 6.75 GHz are from other qubit-oscillator circuits that are coupled to the transmission line and can be ignored here.

Numerically calculated values for the ground-state entanglements \mathcal{E}_{gs} and thermal-equilibrium entanglements \mathcal{E}_{te} for all five sets of spectroscopy data in the three circuits are summarized in Table S1. In all cases, \mathcal{E}_{gs} is quite high while \mathcal{E}_{te} is substantially lower than \mathcal{E}_{gs} due to significant population in the state $|1\rangle$. For circuits I and II, which have similar values of Δ , \mathcal{E}_{te} decreases as g increases, which is explained by the suppression of the qubit frequency at $\varepsilon = 0$ from its bare value (see Fig. S9 and Ref.²⁵):

$$\omega_{01} = \Delta e^{-2a^2}, \quad (\text{S31})$$

and the resulting increase in thermal excitation of the state $|1\rangle$. The relatively high value of \mathcal{E}_{te} for circuit III is due to its large Δ and hence lower population in the state $|1\rangle$. We have calculated \mathcal{E}_{gs} for the parameters of Refs.¹² and¹³ and found that the values are, respectively, 6% and 4%. Note that in calculating \mathcal{E}_{gs} for Ref.¹², out of the different modes of the coplanar waveguide resonator we only consider the mode that is most strongly coupled to the qubit. If we include all the three modes that are relevant to that experiment, we find that the

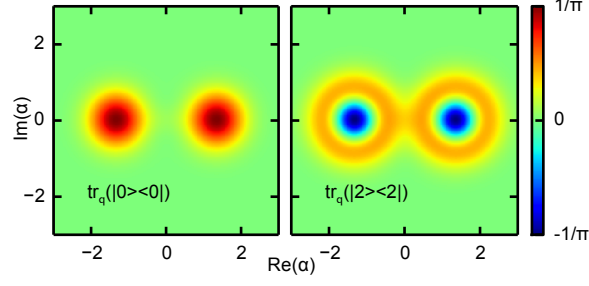


FIG. S7. **The calculated Wigner functions of the reduced density operators of the oscillator.** The left and right hand side of the panels shows the Wigner functions of the reduced density operators of the oscillator $\text{tr}_q(|0\rangle\langle 0|)$ and $\text{tr}_q(|2\rangle\langle 2|)$, respectively, in the case of circuit II. The states $|0\rangle$ and $|2\rangle$ are calculated from $\mathcal{H}_{\text{total}}$ using the parameters in Table I in the main text, and tr_q is the partial trace over qubit states.

entanglement between the qubit and the three harmonic oscillators combined is 11%.

Although \mathcal{E}_{gs} and \mathcal{E}_{te} can be evaluated by numerical calculation, it is worth deriving approximate expressions for them, which gives a more intuitive picture of the qubit-oscillator entanglement. The qubit-oscillator ground state at $\varepsilon = 0$ can be approximated as

$$|0\rangle = \frac{1}{\sqrt{2}} \left(|L\rangle_q \otimes |-\alpha\rangle_o + |R\rangle_q \otimes |\alpha\rangle_o \right). \quad (\text{S32})$$

Taking into consideration the fact that $\langle \alpha | -\alpha \rangle = e^{-2\alpha^2}$, the qubit's reduced density matrix is given by

$$\rho_q = \frac{1}{2} \begin{pmatrix} 1 & e^{-2\alpha^2} \\ e^{-2\alpha^2} & 1 \end{pmatrix}. \quad (\text{S33})$$

The eigenvalues of ρ_q are then $(1 \pm e^{-2\alpha^2})/2$. The entanglement can be evaluated using Eq. (S29):

$$\mathcal{E}_{\text{gs}} = -\frac{1}{2} \left(1 + e^{-2\alpha^2} \right) \log_2 \left(\frac{1 + e^{-2\alpha^2}}{2} \right) - \frac{1}{2} \left(1 - e^{-2\alpha^2} \right) \log_2 \left(\frac{1 - e^{-2\alpha^2}}{2} \right), \quad (\text{S34})$$

which when expanded to second order in $e^{-2\alpha^2}$ gives

$$\mathcal{E}_{\text{gs}} \simeq 1 - \frac{1}{2 \ln 2} e^{-4\alpha^2}. \quad (\text{S35})$$

Figure S8 shows the entanglement calculated based on the approximate expression for the ground state Eq. (S32), with and without the small $e^{-2\alpha^2}$ approximation, along with the

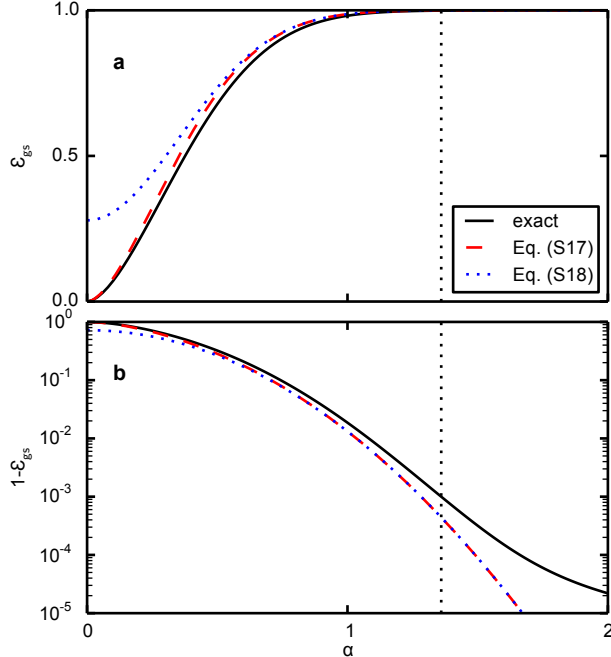


FIG. S8. **The qubit-oscillator entanglement as a function of α .** The entanglement is calculated from Eq. (S34) (red dashed line), Eq. (S35) (blue dotted line), and a numerical diagonalization of the Rabi model Hamiltonian using the parameters Δ and ω_o from circuit II in our experiment (black solid line). Panel **a** shows the linear plot of \mathcal{E}_{gs} while panel **b** shows the log plot of $1 - \mathcal{E}_{\text{gs}}$. The black dotted line indicates the displacement of circuit II, i.e. $\alpha = 1.36$. Both Eq. (S34) and Eq. (S35) slightly overestimate the entanglement when $\alpha > 1.5$, where the entanglement is around 99.9% or higher. Since Eq. (S35) is derived by assuming a large value of α , it is not valid when $\alpha < 0.5$.

entanglement obtained for the numerically calculated (and essentially exact) ground state. For the parameters of circuit II, Eqs. (S34) and (S35) give an entanglement of 99.94% while the exact calculation gives the value 99.88%.

Equation (S35) is a poor approximation for $\alpha < 0.5$, because when we expanded the logarithm in a Taylor series we assumed a small value of $e^{-2\alpha^2}$. Figure S8 suggests that Eqs. (S34) and (S35) deviate from the exact result for $\alpha > 1.5$ as well. It should be noted, however, that the absolute value of the error in these approximate expressions decreases monotonically and approaches zero as $\alpha \rightarrow \infty$. It is only when the error is compared to the rapidly decreasing quantity $1 - \mathcal{E}_{\text{gs}}$ that the approximate expressions seem to deviate from the exact result for large values of α .

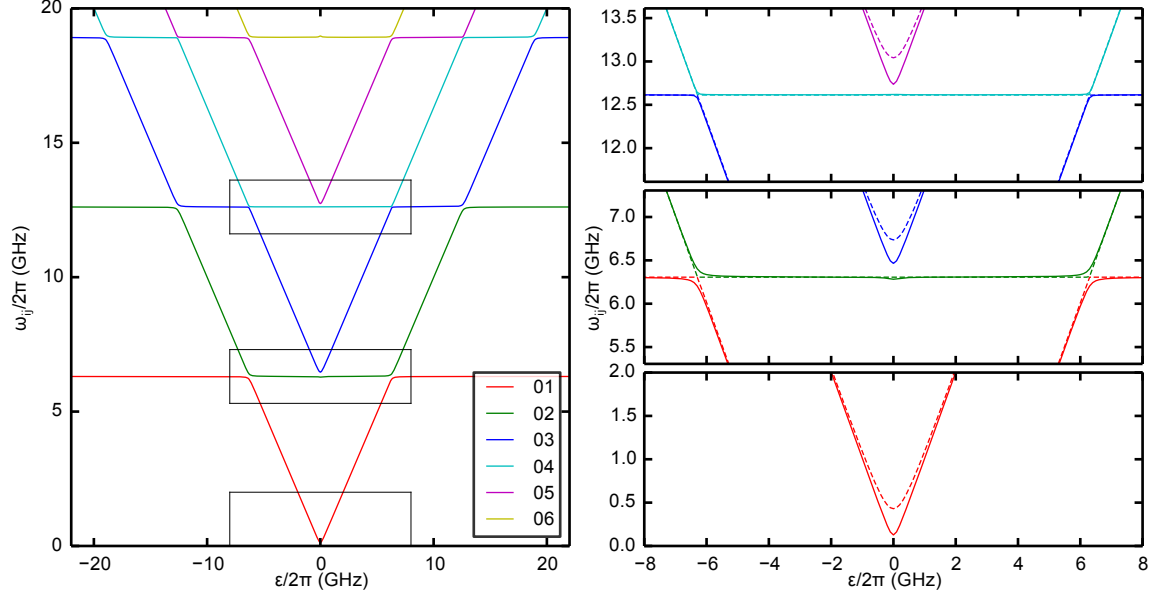


FIG. S9. **The calculated transition frequencies from the ground state ω_{0i}^{cal} as functions of ε .** The parameters of the circuit I at $n_{\phi_q} = -1.5$, i.e., $\Delta/2\pi = 0.430$ GHz, $\omega_o/2\pi = 6.306$ GHz, and $g/2\pi = 4.92$ GHz, are used for the calculation. The three right panels, where ω_{0i}^{cal} in the non-interacting case $g = 0$ are also plotted in dashed lines, are the magnifications of the three rectangles in the left panel.

It can also be seen in Fig. S8 that the approximate expression Eq. (S32) leads to an overestimation of the entanglement. This overestimation is due to the fact that Eq. (S32) is obtained by ignoring the σ_x term in the Hamiltonian (except for its role in identifying the symmetric superposition as the ground state of the coupled system). Because this term does not contain oscillator operators, it favours having a superposition of the states $|L\rangle_q$ and $|R\rangle_q$ with the state of the oscillator being independent of the state of the qubit. It therefore favours a slightly increased overlap (in the state of the oscillator) between the two branches of the superposition than the overlap present in Eq. (S32), and the increased overlap leads to a reduction in the entanglement.

A quick estimate for the entanglement in the thermal-equilibrium state \mathcal{E}_{te} can be obtained by taking the product

$$\mathcal{E}_{\text{te}} \simeq \mathcal{E}_{\text{gs}} \times (p_0 - p_1) = \left(1 - \frac{e^{-4\alpha^2}}{2 \ln 2}\right) \times \tanh\left(\frac{\hbar\Delta e^{-2\alpha^2}}{2k_{\text{B}}T}\right), \quad (\text{S36})$$

where p_0 and p_1 are, respectively, the occupation probabilities of the states $|0\rangle$ and $|1\rangle$, and k_{B}

Table S1. **Parameters obtained from fitting spectroscopy measurements and calculated entanglement.**

circuit	n_{Φ_q}	$\Delta/2\pi$ (GHz)	$\omega_o/2\pi$ (GHz)	$g/2\pi$ (GHz)	\mathcal{E}_{gs}	$p_0 - p_1$	\mathcal{E}_{te}
I	-0.5	0.505	6.336	4.57	89%	0.095	7.3%
I	-1.5	0.430	6.306	4.92	92%	0.068	5.5%
I	2.5	0.299	6.233	5.79	97.2%	0.028	2.6%
II	-0.5	0.441	5.711	7.63	99.88%	0.0066	0.90%
III	0.5	3.84	5.588	5.63	91%	0.26	25%

The parameters are obtained from five sets of spectroscopy data in three circuits. The ground-state qubit-oscillator entanglement \mathcal{E}_{gs} and the thermal-equilibrium entanglement \mathcal{E}_{te} are calculated numerically using the energies and energy eigenstates obtained using Hamiltonian diagonalization and are essentially exact. In the calculations of $p_0 - p_1$ and \mathcal{E}_{te} , $T = 45$ mK is used.

is the Boltzmann constant. When $\alpha = 0$, one obviously has $\mathcal{E}_{\text{te}} = \mathcal{E}_{\text{gs}} = 0$ (although the right-most part of Eq. (S36) gives a finite value because it contains a poor approximation for \mathcal{E}_{gs} in that limit). On the other hand, when α increases to very large values, \mathcal{E}_{gs} approaches one but $p_0 - p_1$ approaches zero. As a result, there is an optimal value of α that balances between maximizing the ground-state entanglement and maximizing the ground-state occupation probability.

Although the above estimate for the thermal-equilibrium entanglement might seem very hand-waving, it turns out to be a rather good estimate, especially in the limits of large \mathcal{E}_{gs} or large $p_0 - p_1$. For example, if we consider a statistical mixture of two complementary two-qubit Bell states, e.g. $(|1\rangle \otimes |0\rangle \pm |0\rangle \otimes |1\rangle)/\sqrt{2}$, with probabilities p_0 and p_1 , the negativity multiplied by two takes the simple form

$$2\mathcal{N} = |p_0 - p_1|. \quad (\text{S37})$$

As a result, our estimate is rather accurate when α is large and therefore \mathcal{E}_{gs} is very close to one, because in this limit the overlap between the oscillator states $|\alpha\rangle$ and $|-\alpha\rangle$ approaches zero and the lowest two energy eigenstates do indeed form a pair of complementary Bell states. Similarly, if we take the opposite limit where $\hbar\omega_{01} \gg k_B T$ and $p_0 - p_1$ is close to one, thermal population of the excited states can be ignored, and the ground-state entanglement \mathcal{E}_{gs} becomes a good estimate for the thermal-equilibrium entanglement.

Before concluding, it is worth pointing out here the difference between the coefficient 4 inside the exponent in Eq. (S35) and the coefficient 2 inside the exponent in Eq. (S31).

The entanglement therefore approaches 100% much faster than ω_{01} approaches zero. This property is desirable for future designs to achieve a high thermal-equilibrium entanglement.

* fumiki@nict.go.jp; These authors contributed equally to this work.

† tfuse@nict.go.jp; These authors contributed equally to this work.

‡ semba@nict.go.jp

§ sashhab@qf.org.qa

- ¹ Wineland, D. J. & Itano, W. M. Spectroscopy of a single Mg⁺ ion. *Phys. Lett. A* **82**, 75–78 (1981).
- ² Haroche, S. & Raimond, J. M. Cavity quantum electrodynamics. *Scientific American* **268**, 54–60. (1993).
- ³ Brune, M. *et al.* Quantum Rabi Oscillation: A Direct Test of Field Quantization in a Cavity. *Phys. Rev. Lett.* **76**, 1800–1803 (1996).
- ⁴ Raimond, J. M., Brune, M. & Haroche, S. Manipulating quantum entanglement with atoms and photons in a cavity. *Reviews of Modern Physics* **73**, 565–582 (2001).
- ⁵ Mabuchi, H. & Doherty, A. C. Cavity quantum electrodynamics: coherence in context. *Science* **298**, 1372–1377 (2002).
- ⁶ Walls, D. F. & Milburn, G. J. Quantum optics (Springer Science & Business Media, 2007).
- ⁷ Nakamura, Y., Pashkin, Yu. A. & Tsai, J. S. Coherent control of macroscopic quantum states in a single-Cooper-pair box. *Nature (London)* **398**, 786–788 (1999).
- ⁸ Clarke, J. & Wilhelm, F. K. Superconducting quantum bits. *Nature (London)* **453**, 1031–1042 (2008).
- ⁹ Chiorescu, I. *et al.* Coherent dynamics of a flux qubit coupled to a harmonic oscillator. *Nature (London)* **431**, 159–162 (2004).
- ¹⁰ Wallraff, A. *et al.* Strong coupling of a single photon to a superconducting qubit using circuit quantum electrodynamics. *Nature (London)* **431**, 162–167 (2004).
- ¹¹ Devoret, M., Girvin, S. & Schoelkopf, R. Circuit-QED: How strong can the coupling between a Josephson junction atom and a transmission line resonator be? *Ann. Phys. (Leipzig)* **16**, 767–769 (2007).
- ¹² Niemczyk, T. *et al.* Circuit quantum electrodynamics in the ultrastrong-coupling regime. *Nature*

- Phys.* **6**, 772–776 (2010).
- ¹³ Forn-Diaz, P. *et al.* Observation of the Bloch-Siegert Shift in a Qubit-Oscillator System in the Ultrastrong Coupling Regime. *Phys. Rev. Lett.* **105**, 237001 (2010).
- ¹⁴ Hepp, K. & Lieb, E. H. On the Superradiant Phase Transition for Molecules in a Quantized Radiation Field : the Dicke Maser Model. *Ann. Phys. (NY)* **76**, 360–404 (1973).
- ¹⁵ Casanova, J., Romero, G., Lizuain, I., Garca-Ripoll, J. J. & Solano, E. Deep Strong Coupling Regime of the Jaynes-Cummings Model. *Phys. Rev. Lett.* **105**, 263603 (2010).
- ¹⁶ Rzążewski K., Wódkiewicz K. & Żakowicz W. Phase Transitions, Two-Level Atoms, and the A^2 Term. *Phys. Rev. Lett.* **35**, 432–434 (1975).
- ¹⁷ Nataf, P., & Ciuti, C. No-go theorem for superradiant quantum phase transitions in cavity QED and counter-example in circuit QED. *Nature Commun.* **1**, 72 (2010).
- ¹⁸ Viehmann, O., von Delft, J., & Marquardt, F. Superradiant phase transitions and the standard description of circuit QED. *Phys. Rev. Lett.* **107**, 113602 (2011).
- ¹⁹ Mooij, J. E. *et al.* Josephson Persistent-Current Qubit. *Science* **285**, 1036–1039 (1999).
- ²⁰ Rabi, I. I. Space quantization in a gyrating magnetic field. *Phys. Rev.* **51**, 652 (1937).
- ²¹ Shimoda, K., Wang, T. C. & Townes, C. H. Further aspects of maser theory. *Phys. Rev.* **102**, 1308–1321 (1956).
- ²² Jaynes, E. T. & Cummings, F. W. Comparison of quantum and semiclassical radiation theories with application to the beam maser. *Proc. IEEE* **51**, 89–109 (1963).
- ²³ Braak, D. Integrability of the Rabi Model. *Phys. Rev. Lett.* **107**, 100401 (2011).
- ²⁴ Bourassa, J. *et al.* Ultrastrong coupling regime of cavity QED with phase-biased flux qubits. *Phys. Rev. A* **80**, 032109 (2009).
- ²⁵ Ashhab, S. & Nori, F. Qubit-oscillator systems in the ultrastrong-coupling regime and their potential for preparing nonclassical states. *Phys. Rev. A* **81**, 042311 (2010).
- ²⁶ Lamb, W. E. & Retherford, R. C. Fine structure of the hydrogen atom by a microwave method. *Phys. Rev.* **72**, 241–243 (1947).
- ²⁷ Forn-Diaz, P. *et al.* Ultrastrong coupling of a single artificial atom to an electromagnetic continuum in the nonperturbative regime. *Nature Phys.* **13**, 39–43 (2017).
- ²⁸ J. R. Johansson, P. D. Nation, and F. Nori, *Comp. Phys. Comm.* **184**, 1234 (2013).
- ²⁹ Hopfield, J. J. Theory of the contribution of excitons to the complex dielectric constant of crystals. *Phys. Rev.* **112**, 1555–1567 (1958).

³⁰ Horodecki, R., Horodecki, P., Horodecki, M. & Horodecki, K. Quantum entanglement. *Rev. Mod. Phys.* **81**, 865–942 (2009).